Yan, R., Zhima, Z., Xiong, C., Shen, X., Huang, J., Guan, Y., Zhu, X., Liu, C. (2020): Comparison of electron density and temperature from the CSES satellite with other space-borne and ground-based observations. - Journal of Geophysical Research: Space Physics, 125, 10, e2019JA027747.

https://doi.org/10.1029/2019JA027747

JGR Space Physics

TECHNICAL REPORTS: DATA
10.1029/2019JA027747

Comparison of Electron Density and Temperature From the CSES Satellite With Other Space-Borne and Ground-Based Observations

Rui Yan[1], Zeren Zhima[1], Chao Xiong[2], Xuhui Shen[1], Jianping Huang[1], Yibing Guan[3], Xinghong Zhu[4], and Chao Liu[3]

[1]National Institute of Natural Hazards, Ministry of Emergency Management of China, Beijing, China, [2]GFZ German Research Centre for Geosciences, Potsdam, Germany, [3]National Space Science Center, Chinese Academy of Sciences, Beijing, China, [4]DFH Satellite Co. Ltd., Beijing, China

Key Points:

- Although there exist scaling factors of the absolute *Ne*/*Te* values between CSES and Swarm, their relative variations are quite consistent
- The large-scale ionospheric structures, such as EIA, WN3/4, WSA, MSNA and MIT, are well represented by the CSES measurements
- It is clear that CSES LAP has the good performance to provide reliable scientific data

Correspondence to:
X. Shen,
shenxh@seis.ac.cn

Citation:
Yan, R., Zhima, Z., Xiong, C., Shen, X., Huang, J., Guan, Y., et al. (2020). Comparison of electron density and temperature from the CSES satellite with other space-borne and ground-based observations. *Journal of Geophysical Research: Space Physics*, *125*, e2019JA027747. https://doi.org/10.1029/2019JA027747

Received 6 JAN 2020
Accepted 13 JUL 2020
Accepted article online 14 AUG 2020

Abstract In this paper we provide a comprehensive comparison of in situ electron density (*Ne*) and temperature (*Te*) measured by Langmuir probe (LAP) on board the China Seismo-Electromagnetic Satellite (CSES), with nearly simultaneous measurements from the Swarm B satellite, incoherent scatter radar (ISR) at Millstone Hill, as well as predictions from empirical models including the incoherent scatter radar ionospheric model (ISRIM) for Millstone Hill and International Reference Ionosphere model (IRI-2016). Results reveal that the global distributions and their relative variations of *Ne*/*Te* from CSES and Swarm are quite consistent during conjunction periods of the two satellites, although the absolute values of Swarm *Ne* are proportionally larger than that of CSES. The large-scale ionospheric structures, such as the equatorial ionization anomaly (EIA), the longitudinal wave number (WN3/4), the Weddell Sea anomaly (WSA), the northern midlatitude summer nighttime anomaly (MSNA), and the midlatitude ionospheric trough (MIT), are well represented by the CSES measurements. For the temporal variation over Millstone Hill station, CSES *Ne* at nightside shows some different characteristics from the predictions of IRI and ISRIM, possibly due to the influences of MIT and midlatitude arc (MLA) that are often observed at latitudes of Millstone Hill. Our results suggest that the CSES in situ plasma parameters are reliable with a high scientific potential for investigation of geophysics and space physics.

1. Introduction

Electron density (*Ne*) and temperature (*Te*) are two key parameters that characterize the status of ionospheric plasma (e.g., Hargreaves, 1992; Lomidze et al., 2018; Schunk & Nagy, 2009). They have been measured since the 1960s by rockets, satellites, and ground-based remote sensing facilities (Kakinami et al., 2013). Currently, the instruments mostly used to measure *Ne*/*Te* include the Langmuir probes, incoherent scatter radars (ISRs), and ionosondes. The measuring mechanisms and data processing methods of *Ne*/*Te* rely on certain assumptions and approximations; therefore, each instrument has its own strengths and limitations (Lomidze et al., 2018). The Langmuir probe works as a conductor immersed in plasma, with a bias voltage applied to it; the derived current is collected as a function of the applied voltage, then to acquire the current-voltage (I-V) characteristic of the probe (e.g., Chen, 2002; Langmuir & Mott-Smith, 1924). Because the Langmuir probe is prone to be contaminated by water vapor or other causes (Lebreton et al., 2006; Oyama, 2015; Oyama et al., 2012; Oyama & Hirao, 1976), further validation is required to guarantee the data quality.

Comprehensive comparison with other similar types of well-calibrated ground- and space-borne data is a conventional validation approach for a new satellite-borne Langmuir probe. The revealed discrepancies can provide helpful information for improving the data quality of a new satellite mission. For example, the *Ne* measured by Challenging Mini-satellite Payload (CHAMP) has been validated by comparison with ionosonde measurements at Jicamarca (McNamara et al., 2007), and the *Te* measurement has been compared with ISR observations located at Arecibo and Tromsø (Rother et al., 2010). The Constellation Observing System for Meteorology Ionosphere and Climate (COSMIC) radio occultation *Ne* was compared_ with those obtained via the CHAMP and Communications/Navigation Outage Forecasting System (C/NOFS) satellites (Pedatella et al., 2015), and the correlation coefficients of in situ observations

from COSMIC, CHAMP, and C/NOFS are both greater than 0.90, indicating an overall good agreement of *Ne* among the three satellite missions. Lomidze et al. (2018) validated the Swarm in situ *Ne* and *Te* by using ground-based radars and COSMIC measurements, and the adjustment based on Swarm-ISRs comparison has improved the data quality of Swarm.

In another way, the comparative analysis on the new measurements with those already known characteristics of ionosphere can also serve as an indirect verification. For example, Kakinami et al. (2011) examined the dayside ionospheric longitudinal structures of *Ne* and *Te* measured by the Hinotori and DEMETER satellites and found that the observed longitudinal structures from these two satellites show similar patterns of wave number-3 (WN3) in December and wave number-4 (WN4) in September, which also have been discussed by other publications (e.g., Immel et al., 2006; Lühr et al., 2012; Xiong & Lühr, 2013). Ryu et al. (2016) investigated the seasonal and spatial variations of in situ observations in topside ionosphere during the solar minimum in 2008–2009 using measurements from CHAMP, Detection of Electro Magnetic Emissions Transmitted from Earthquake Regions (DEMETER), and Defense Meteorological Satellite Program (DMSP) F-15 satellite. Results from all these satellites show quite consistent large-scale ionospheric structures, for example, the equatorial ionization anomaly (EIA) with longitudinal asymmetry of WN3 and WN4 patterns at different seasons, the Weddell Sea anomaly (WSA), and the northern midlatitude summer nighttime anomaly (MSNA), although with slight altitude dependence. The equatorial plasma temperature anomaly (EPTA), which is the anomaly of *Te* at the topside ionosphere during the evening-midnight period, observed by the Hinotori satellite shows quite consistent feature with the simulation from Sheffield University Plasmasphere Ionosphere Model (SUPIM) (Balan et al., 1997). Matyjasiak et al. (2016) studied the seasonal variations of the nightside midlatitude ionospheric trough (MIT) observed by DEMETER and COSMIC and found that the typical magnetic latitude (MLAT) of MIT minimum is at ±62° during magnetically quiet period, while under magnetically disturbed period the trough minimum moves equatorward as far as 5°. Zhang et al. (2013) first reported the midlatitude arc (MLA) by using airglow emission (OI 135.6 nm) measured by the Thermosphere, Ionosphere, Mesosphere, Energetics and Dynamics/Global Ultraviolet Imager (TIMED/GUVI), and they found that the MLA can be observed in all seasons under geomagnetically quiet period ($Kp < 1.0$) and low solar activity conditions, with clear seasonal dependence, that is, during equinoxes the MLA can be observed in both hemispheres, while during solstices, it is only observed in the winter hemisphere. Li et al. (2018) found similar nighttime midlatitude enhancements from the CHAMP and DMSP in situ measurements. Zhong et al. (2019) also found that at approximately ±40° MLAT, the nighttime *Ne* derived from COSMIC is generally greater than the adjacent MLAT, especially in the topside ionosphere. Such nightside *Ne* enhancements at midlatitude have been confirmed by the observations from Swarm satellites (Xiong et al., 2019). Liu et al. (2015) revealed the anticorrelation between *Te* and *Ne* at the WSA region in both day and night times, by using concurrent measurements from Tatiana-2, DEMETER, and F3/COSMIC covering altitude of 660–830 km. In addition to the observations, the empirical or physical models have also been widely used for providing the ionospheric background information. However, the model predication values are not very precise; for example, the international reference ionosphere (IRI) model generally overestimates the *Ne* at topside ionosphere during low solar minimum condition, whereas the *Te* estimates are somehow lower than the satellite observations (Kakinami et al., 2013; Lühr & Xiong, 2010; Xiong et al., 2013; Zhang, 2014).

The China Seismo-Electromagnetic Satellite (CSES), launched on 2 February 2018, is the first space-based platform of China for earthquake observations and geophysical field measurements (Shen et al., 2018). Eight types of scientific payloads are equipped to provide a continuous survey of the ionospheric plasma, background magnetic field and electromagnetic waves, and energetic particles. Among them, the Langmuir probe (LAP) measures *Ne* and *Te* within the range of 5×10^8–1×10^{13} m^{-3} and 500–10,000 K, respectively. The preliminary application of the CSES *Ne* and *Te* has been presented, for example, Yan, Guan et al. (2018) and Yan, Shen et al. (2018). The primary aim of this paper is to evaluate the reliability of CSES LAP measurements. It is relevant to mention that a statistical comparison between CSES plasma data set with other independent data sources has not been performed before. In this study, we provide a comprehensive comparison between CSES and other space-borne and ground-based measurements (e.g., coincident measurements from Swarm B satellite and the ISR measurements at Millstone Hill). In addition, model predictions, for example, from IRI, have also been applied. In section 2, we briefly describe the LAP data and other data set used in this paper. Sections 3 and 4 present the comprehensive comparisons of *Ne*/*Te* between

different data sources. In section 5, we provide relevant discussion, and in section 6, we summarize the main findings of this study.

2. Data Sources and Simultaneous Measurements Selection

2.1. Data Sources

The *Ne*/*Te* obtained from the CSES, Swarm B, ISR at Millstone Hill station, predictions by the IRI-2016 model, and the incoherent scatter radar ionospheric model (ISRIM) for Millstone Hill (Zhang et al., 2005) were used in this paper.

CSES is a Sun-synchronous orbit satellite at an altitude of 507 km with a descending node of 14:00 local time (LT). The spherical sensor of LAP is installed on the 50 cm extension boom to reduce the interference from the platform. The collected current changes with the sweeping voltage applied to the sensor. The relationship between the sweeping voltage and the sensor current is determined by the I-V characteristic curve through which the *Ne* and *Te* are obtained. Each sweeping period contains three parts: voltage down-sweeping, voltage up-sweeping, and fixed bias voltage sweeping. The voltage down-sweeping is subject to interference and is used to check whether the probe is contaminated or not. The fixed biased voltage sweeping only measures the relative variation of current and voltage instead of *Ne*/*Te*. *Ne*/*Te* is calculated from voltage upsweeping. LAP operates in the survey and burst modes (over China and seismic belts). The resolution of LAP is 3 seconds in the survey mode and 1.5 seconds in the burst mode (Liu et al., 2018).

The Swarm satellites (A, B, and C) were launched on 22 November 2013. A pair of LAPs is installed on each of the Swarm satellites (Haagmans et al., 2004). In this paper, we used the observations from Swarm B to compare with CSES ones, as they have the closest altitude. Usually, the current between the probe and the satellite is measured by the varying probe bias in small steps over the complete range of values that could possibly be relevant (Lebreton et al., 2006). However, a different method was chosen for providing the bulk of Langmuir probe measurements on board the Swarm. By tracking a specific current on board, only three bias points are selected at values that are most relevant for determining plasma parameters. At these points, the bias voltage is modulated by using a harmonic signal with small amplitude. The current and the complex admittance are measured at each of three points, which is sufficient to estimate the density, temperature, and potential (Knudsen et al., 2017). Lomidze et al. (2018) has provided a linear correction method for the Swarm *Ne* and *Te*. In this study, we applied the linear correction to *Ne* and *Te* of Swarm B, based on equations (2) and (5) of Lomidze et al. (2018), before analysis and comparison.

In this paper, the data obtained by the ISR at Millstone Hill were also used. The Millstone Hill ISR system consists of a 2.5 MW peak Ultra High Frequency (UHF) transmitter coupled to a 68-m zenith directed fixed parabola antenna, as well as a fully steerable 46-m antenna. It measures the ionospheric plasma density, temperature, velocity, and composition with high accuracy (Zhang & Holt, 2004). The data from the zenith antenna were used in this study, because the zenith antenna is fixed at an elevation angle of 88°. However, as the ISR operates occasionally, there are only limited measurements available for comparing with CSES. Therefore, we used additional model predictions from the ISRIM (http://models.haystack.mit.edu/models). This model utilizes the radar observations of basic ionospheric parameters to calculate the *Ne*, *Ti*, *Te*, and line-of-sight ion drift (*Vi*). Model-predicted parameters are averaged in cadence of 1 hour local time, 1° step of geographic latitude between 32° and 55° and 50 km step of altitude from 200 to 600 km.

The IRI model provides monthly averages of electron and ion densities and temperatures in the altitude range of 50–2,000 km (Bilitza et al., 2017). In this paper, we use the version of IRI-2016 updated on 26 March 2018. *Ne*Quick is used for the topside *Ne* profile, URSI maps are used to get the F2 peak density (NmF2), the AMTB-2013 model is used to obtain the F2 peak height (hmF2), the ABT-2009 option is used for the bottom side thickness parameter, and TBT-2012 with solar dependence is used for *Ne*.

2.2. Simultaneous Measurements Selection

For comparison, we selected the simultaneous measurements from different data sources. As the LT of CSES is fixed while it slowly drifts for Swarm B (see Figure 1), four conjunction periods are found between the two satellite from May 2018 to October 2019, which are 6–13 July 2018, 18–27 November 2018, 7–16 April 2019, and 27 August–6 September 2019. Unfortunately, the LAP of CSES is temporarily turned off from 18 June to

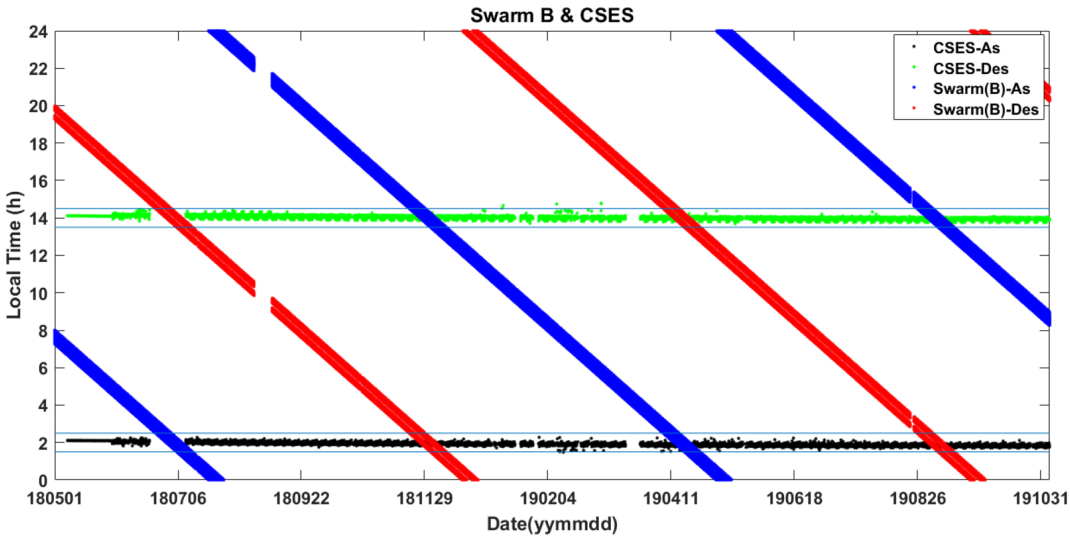

Figure 1. The local time variation of CSES and Swarm B satellites from May 2018 to October 2019. The ascending (As)/descending (Des) orbits of CSES are represented by black and green dots, and the corresponding orbits of Swarm B are denoted by blue and red dots, respectively. The horizontal cyan lines represent the local time window of 14 ± 0.5 h and 02 ± 0.5 h.

11 July, due to in-orbit commission test. So, for the first overlap we just used data during 12–19 July 2018. We compared the observations during these conjunction periods.

To compare the CSES data with measurements obtained by the ISR, the revisiting orbits when CSES passed by (longitudinal difference less than 2.5°) Millstone Hill station (42.5°N, 71.5°W) from May 2018 to November 2019 were considered. In Figure 2, the black star indicates the position of Millstone Hill station, and blue curves represent footprints of the revisiting orbits. For each selected orbit, the coincident measurements of CSES and ISR with time difference less than 15 minutes were used. For each revisiting orbit of CSES above Millstone Hill, we used averages of CSES data within 5.0°/2.5° of latitude/longitude relative to ISR location and the average values of corresponding ISR observations from 485 to 535 km. Finally, we

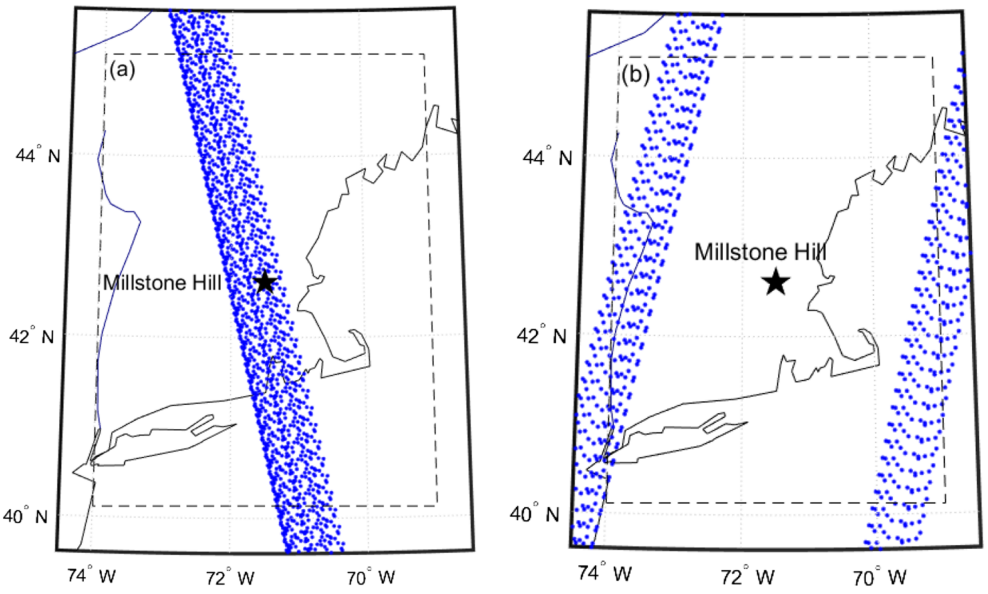

Figure 2. The footprints of CSES passing by Millstone Hill from May 2018 to November 2019. (a) Ascending orbits (nightside); (b) descending orbits (dayside).

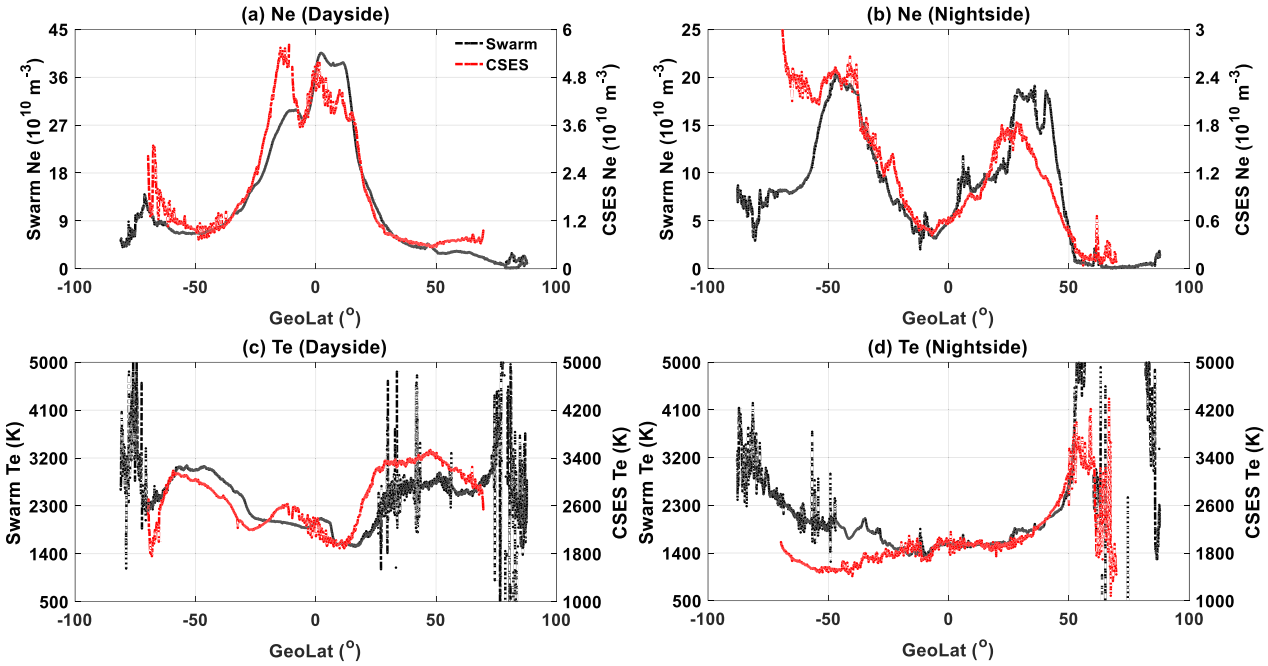

Figure 3. The comparison of *Ne*/*Te* measurements from CSES (red) and Swarm (black) within the closest orbits at closest local time in 25 November 2018.

obtained 22 coincident events between CSES and ISR. The same method was applied for comparing the CSES data with predictions from ISRIM.

3. Simultaneous Measurements Comparison

3.1. CSES and Swarm

Firstly, we compared *Ne*/*Te* measurements between CSES and Swarm during their conjunction periods. Figure 3 shows the latitudinal profiles of *Ne*/*Te* measurements from CSES (red) and Swarm (black) on 25 November 2018 when the two satellites were close to each other. The orbits on dayside (left) and nightside (right) are presented separately. For each subpanel, the values of *Ne*/*Te* from Swarm and CSES are depicted by the left and right *y*-axis, respectively. The measurements of two satellites show very similar latitudinal variations, but the absolute values of Swarm *Ne* are roughly eight times larger (both day and night sides) than those from CSES. The *Te* measurements both from two satellites are basically at the same range.

For each pair of orbits traveled by CSES and Swarm with the closest temporal and spatial separation, the mean values of *Ne*/*Te* within ±45° geographic latitudes are derived separately for the two satellites. These mean values of *Ne* and their linear regression during the first (July 2018, left panels) and fourth (August 2019, right panels) conjunction periods are shown in Figure 4. The red line is the regression line, and the "R" is the correlation coefficient in Figure 4. Quite good linear relation is found between CSES and Swarm *Ne* measurements at both dayside (top panels) and nightside (bottom panels), with correlation coefficients exceeding 0.6 (except the nightside result during July 2018). Similarly, Figure 5 shows the correlations of *Te* between CSES and Swarm B during the first (July 2018, left panels) and fourth (August 2019, right panels) conjunctions. On the dayside, the *Te* measured by the two satellites is quite consistent, with correlation coefficients above 0.7 (Figures 5a and 5b), while on the nightside no clear correlation is visible between the two satellites (Figures 5c and 5d).

The linear regression during all the four conjunction periods is listed out in Table 1, with parameters of the slop and intercept of linear regression, as well as correlation coefficient. As listed out in Table 1, the *Ne* measurements from CSES and Swarm B show quite good correlations during all the four conjunctions (relatively low for the conjunction on April 2019), and the correlation coefficients on dayside are always larger than that on nightside. For dayside *Te*, the correlation coefficients reach over 0.7 except the one during 7–16 April 2019, while for the nightside *Te*, no correlation is visible between the two satellites.

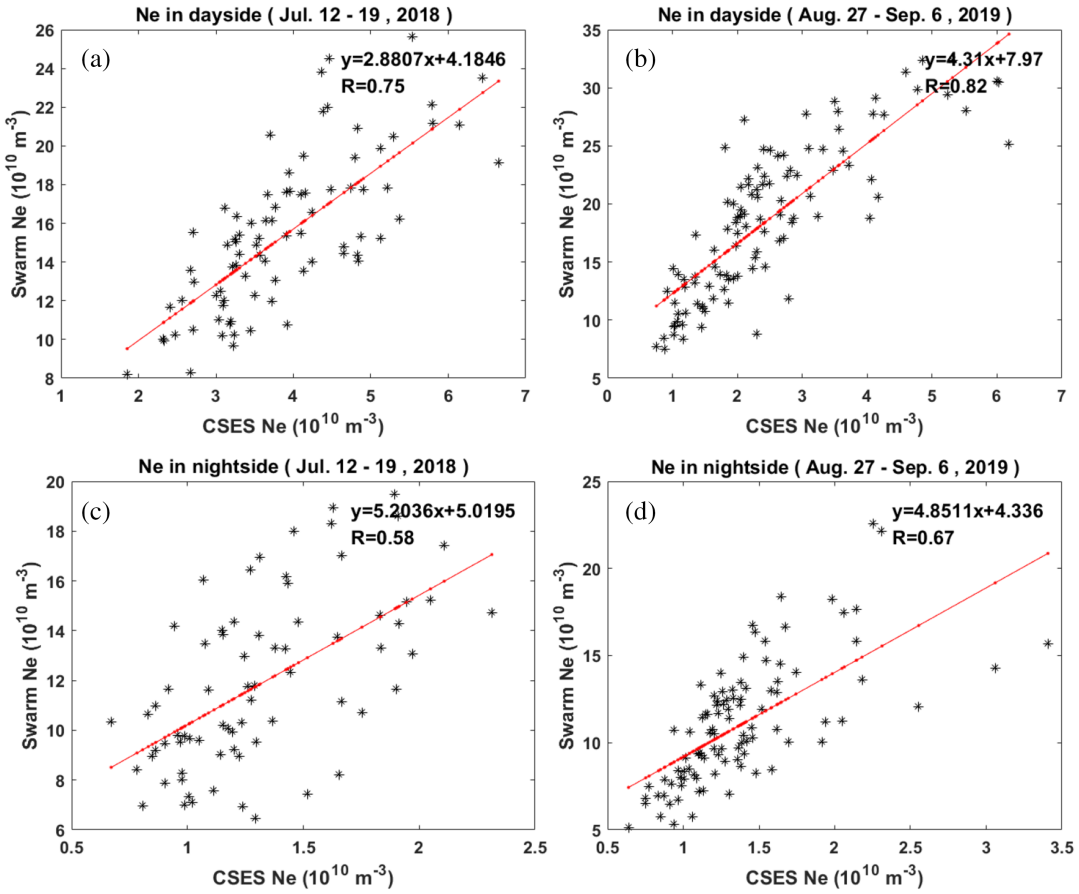

Figure 4. Linear relation between CSES *Ne* and Swarm *Ne* in dayside (a, b) and nightside (c, d) during 12–19 July 2018 (a, c) and 27 August–6 September 2019 (b, d).

3.2. CSES and ISR at Millstone Hill

Based on the criteria for selecting simultaneous measurements between CSES and ISR at Millstone Hill (see section 2.2), only 22 events are found from May 2018 to November 2019. Therefore, instead of showing their correlation, we present their temporal variations in Figure 6. The red dotted lines represent *Ne*/*Te* from CSES, green dotted lines are from ISR, and blue dotted lines are from the ISRIM. The global magnetic activity *Kp* index during all 22 events kept below or equal to 3. It is clearly that the variation trend of CSES *Ne*/*Te* is relatively more stable than that of ISR *Ne*/*Te* (Figure 6). The time of the 22 ISR events is roughly around 19:30 UT, corresponding to the 14:30 LT at Millstone Hill, which matches well with the CSES LT coverage on the dayside. The dayside *Ne* from CSES is nearly 60% lower (on average) than the values of ISR, but the *Te* values from CSES are about several hundred K higher than that measured by ISR.

Figure 7 shows the differences of *Ne* (top panel) and *Te* (bottom panel) between CSES data and ISR (green) as well as ISRIM predicts (blue). In general, the empirical model results are smoother than observations at Millstone Hill; therefore, the difference between ISRIM and CSES measurements is more stable than that between CSES and ISR.

4. Comparisons for Global Distribution and Temporal Variation

4.1. Global Distributions of *Ne*/*Te*

In section 3, we mainly focus on the correlation analysis between CSES and other data sources during conjunction periods. In this section, we compare the global distribution of *Ne*/*Te* derived from CSES and Swarm B.

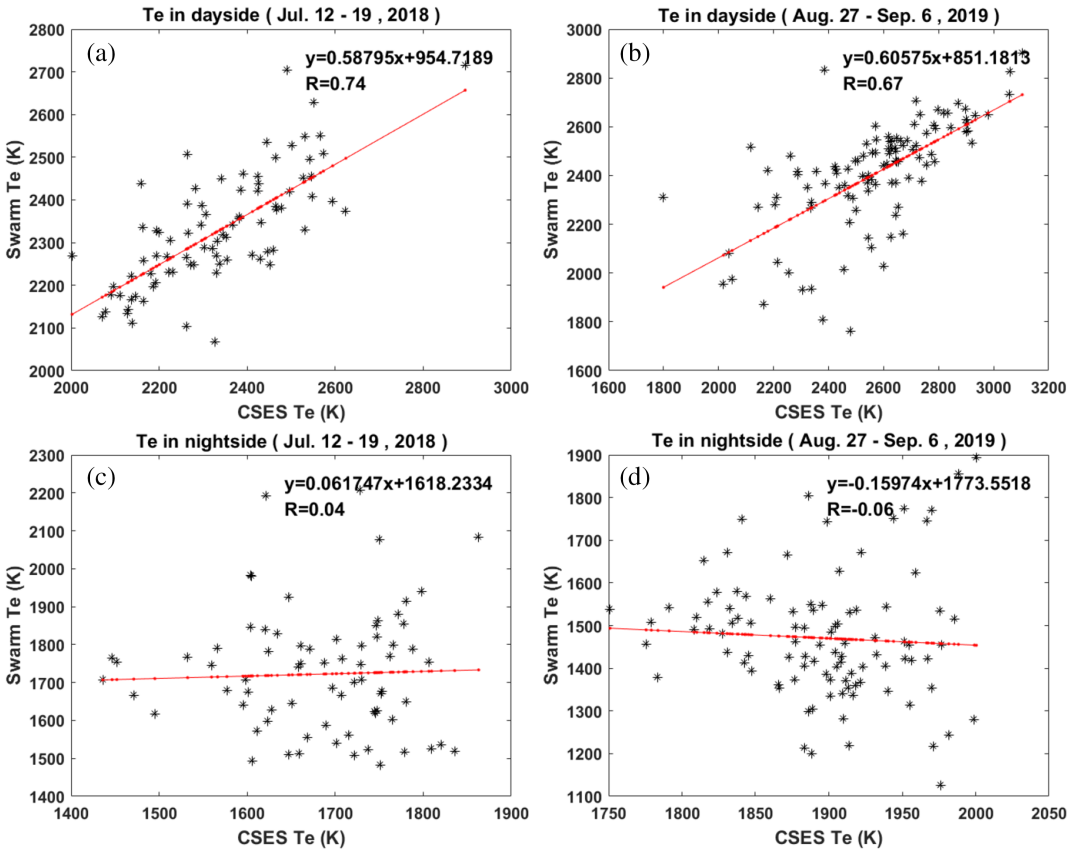

Figure 5. The same as Figure 4 but for *Te*.

For each conjunction period, the observations from CSES and Swarm B are separately sorted into bins of 5° (longitude) × 2.5° (latitude). To reduce the magnetic disturbance influence, only the observations under magnetically quiet conditions ($Kp \leq 3$) were considered. The global distributions of *Ne* are shown in Figures 8 and 9. Since we have given emphasis in the variation analysis of the *Ne/Te* from CSES, and calibration of such parameters is still going on, to let a clear presentation, the scale color bars are not the same in our comparisons. Clear EIA double crests are seen in the Swam B *Ne* on the dayside, while CSES Ne shows only a single crest (Figure 8, marked by black ellipses). The longitudinal WN4 pattern during the conjunction period in July 2018 is clearly seen from both satellites, with four *Ne* maxima located at 0°, 100°, −150°, and −120° longitudes, respectively (marked by black ellipses in Figures 8a and 8d). During the conjunction periods of November 2018 and April 2019, the longitudinal *Ne* distributions at equatorial and low

Table 1
The Correlation Parameters of Ne/Te Between CSES and Swarm B During Four Conjunction Periods

Ne/Te	Correlation parameters	12–19 July 2018	18–27 November 2018	7–16 April 2019	27 August–6 September 2019
Ne (dayside)	Correlation coefficients	0.75	0.81	0.61	0.82
	Slop	2.88	7.72	2.07	4.31
	Intercept ($10^{10}/m^{-3}$)	4.18	1.28	14.40	7.97
Ne (nightside)	Correlation coefficients	0.58	0.69	0.44	0.67
	Slop	5.2	8.22	3.43	4.85
	Intercept ($10^{10}/m^{-3}$)	5.02	0.99	6.01	4.34
Te (dayside)	Correlation coefficients	0.74	0.70	0.20	0.67
	Slop	0.59	0.48	0.30	0.60
	Intercept (*K*)	954.72	796.72	1332.63	851.18
Te (nightside)	Correlation coefficients	0.04	−0.14	−0.16	−0.06
	Slop	0.062	−0.44	−1.34	−0.16
	Intercept (*K*)	1618.23	2576.86	4211.46	1773.55

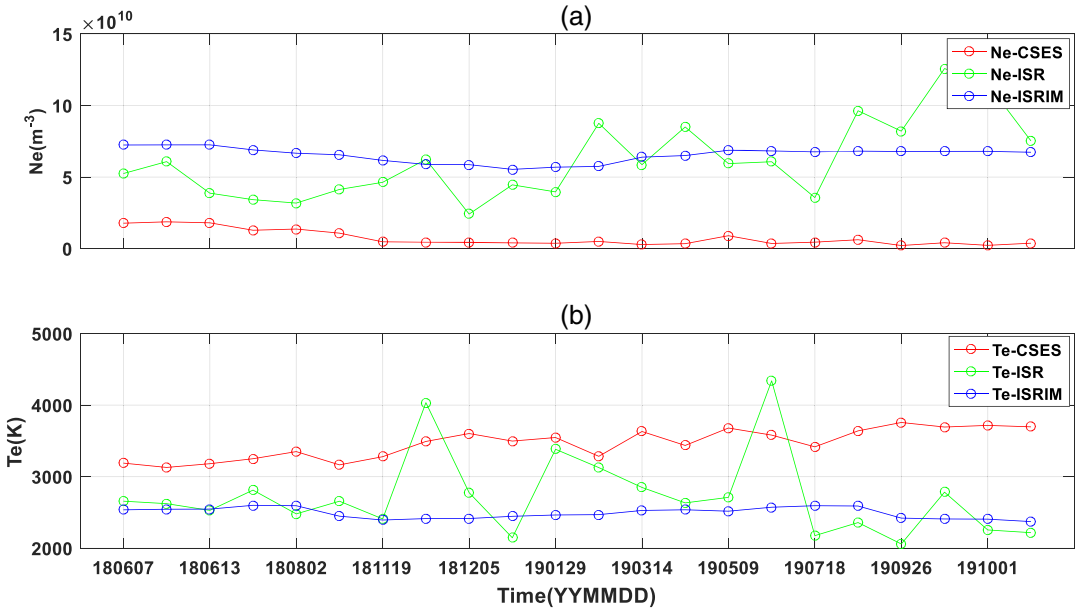

Figure 6. Comparison of simultaneous *Ne* and *Te* obtained by CSES (red), ISR (green), and ISRIM (blue) from May 2018 to November 2019. Panel (a) is the *Ne*; panel (b) is the *Te*.

latitudes exhibit as WN3 structure (Figures 8b and 8c). The seasonal variation of *Ne* longitudinal distribution is mainly caused by the seasonal dependent forcing of various tides and waves propagating from the lower atmosphere (Immel et al., 2006; Lühr et al., 2012; Xiong & Lühr, 2013).

Figure 9 shows the *Ne* distributions of CSES (top) and Swarm B (bottom) on the nightside around 02:00 LT. During July and November 2018, CSES *Ne* depicts clearer WSA and MSNA structures at the middle latitudes than that of Swarm *Ne* (marked by black ellipses in Figures 9a, 9b, 9d, and 9e). While during April 2019, a more prominent feature of *Ne* global distribution is the longitudinal WN3 pattern at low and equatorial

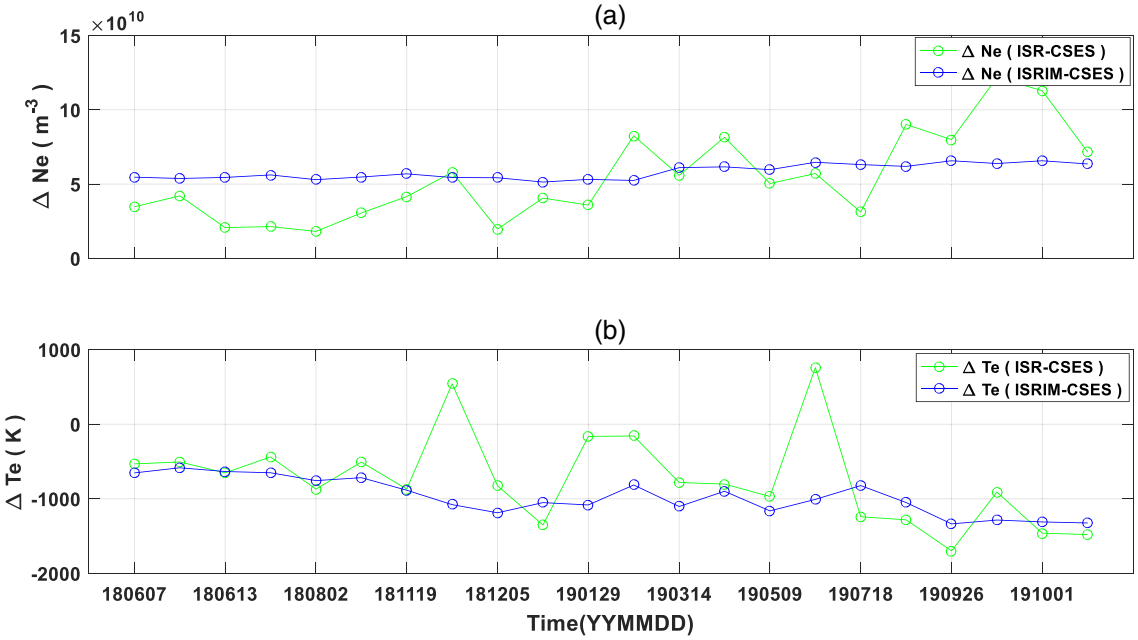

Figure 7. Same as Figure 6 but for difference values of *Ne* (up panel)/*Te* (bottom panel) between CSES and ISR (green) and between CSES and ISRIM (blue).

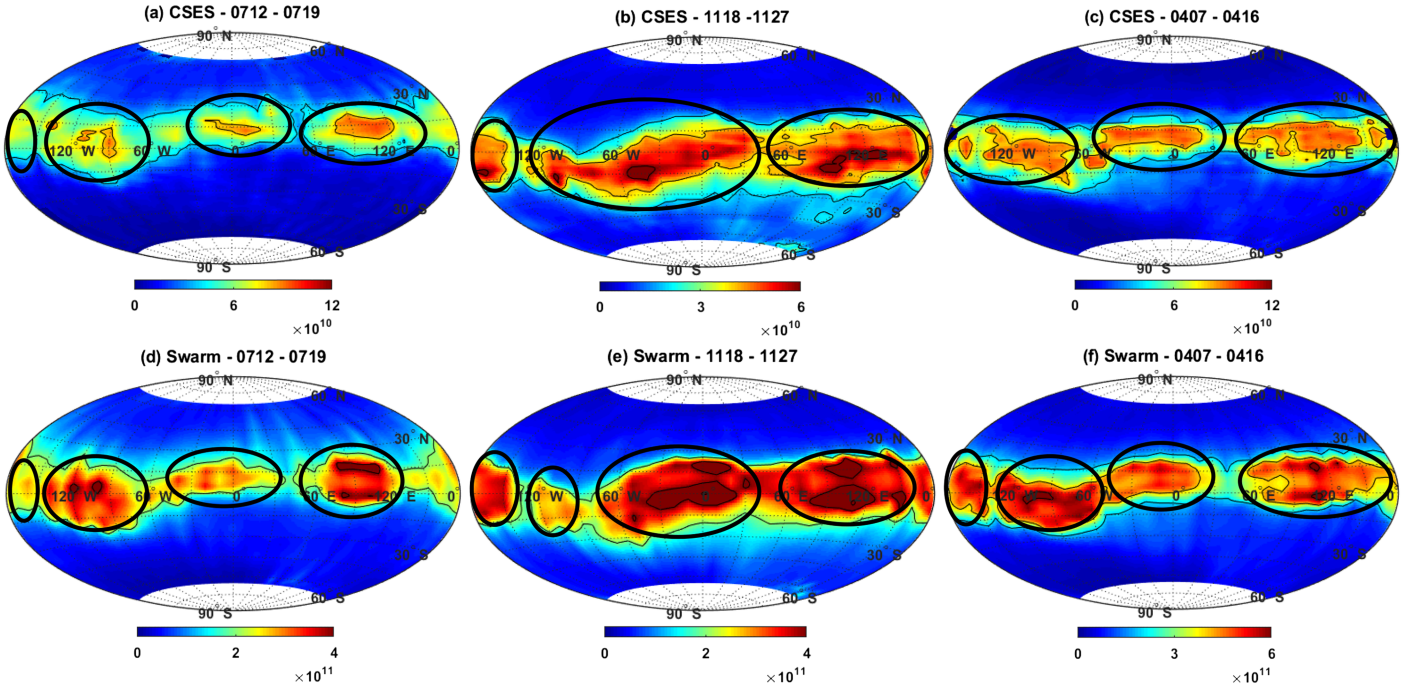

Figure 8. The global distributions of *Ne* at 14:00 LT of CSES (up panels) and Swarm (bottom panels) under the geomagnetic quiet conditions. From left to right: *Ne* measurements during 12–19 July 2018, 18–27 November 2018, and 7–16 April 2019, corresponding to roughly at summer solstice, winter solstice, and spring equinox, respectively.

latitude (denoted by the black ellipse in Figures 9c and 9f). At subauroral region, the MIT is clearly visible between 60°–25°W and 40°–60°N during Northern summer hemisphere (denoted by the red arrows in Figures 9a and 9d), while it can be seen between 30°–100°E and 40°–60°S in Southern summer hemisphere (indicated by the red arrows in Figures 9b and 9e), which are consistent with the results of Matyjasiak

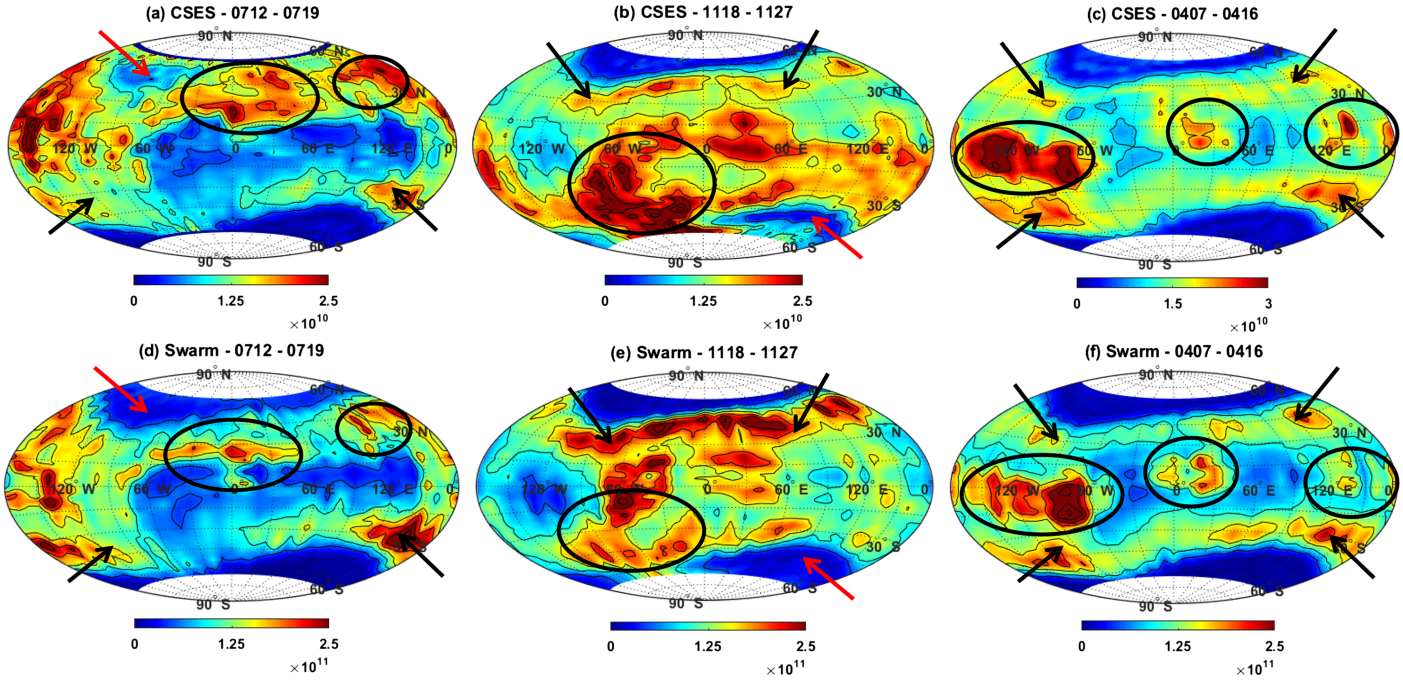

Figure 9. Same as Figure 8 but for *Ne* at 02:00 LT.

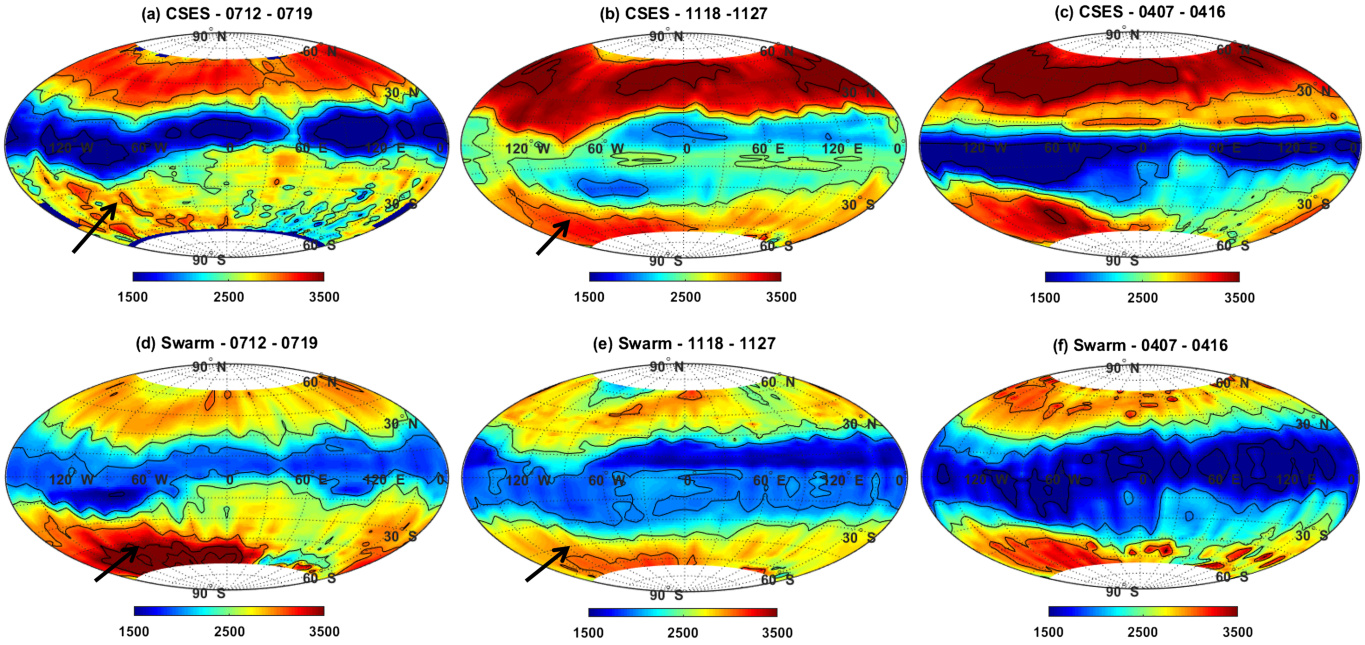

Figure 10. Same as Figure 8 but for *Te* at 14:00 LT.

et al. (2016). Importantly, the structure of MLA is also identified by CSES *Ne* and Swarm *Ne* (denoted by the black arrows in Figure 9), which was earlier reported by Li et al. (2018) from CHAMP (460–350 km) and DMSP (850 km) observations.

For global distribution of *Te* at dayside shown in Figure 10, a clear ETA structure is found at equatorial region, which also shows seasonal variations. A notable feature of *Te* measured by CSES is the abnormal increases/decreases in the dayside/nightside *Te* over the WSA region in November 2018 (marked by black arrows in Figures 10b, 10e, and 11b), which is consistent with previous research (Liu et al., 2015; Ryu et al., 2016). It is worth noting that besides November 2018, a region of relatively high *Te* over WSA region

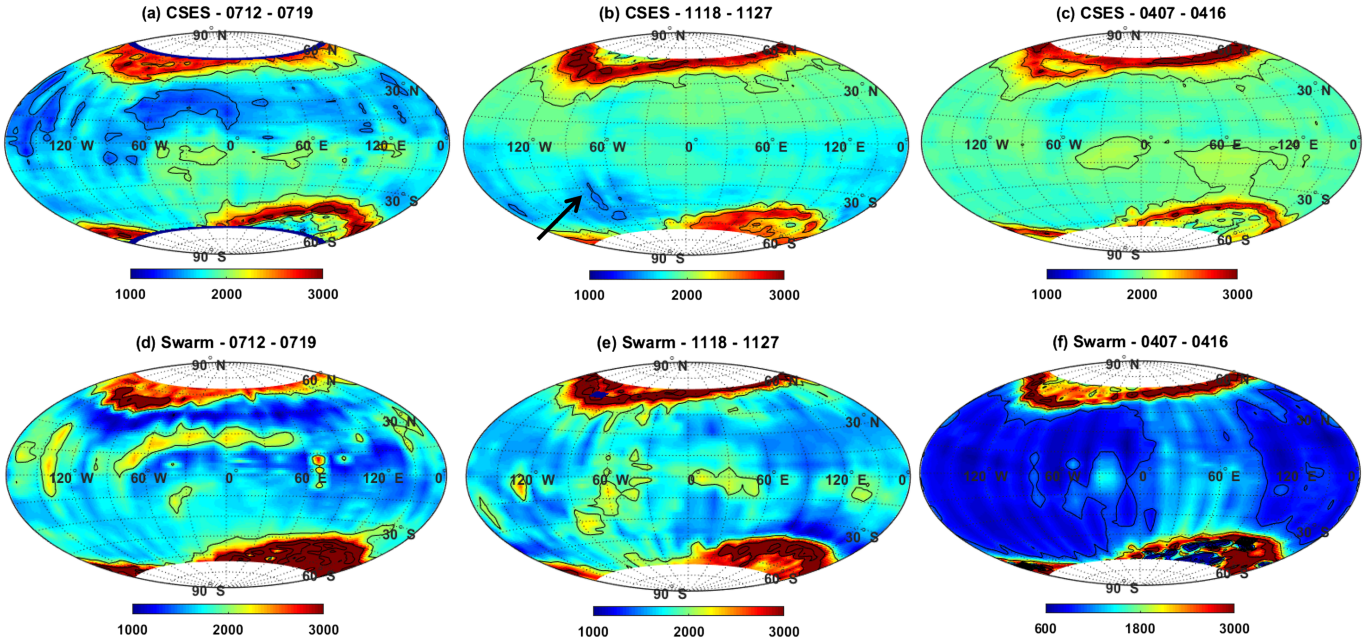

Figure 11. Same as Figure 10 but for *Te* at 02:00 LT.

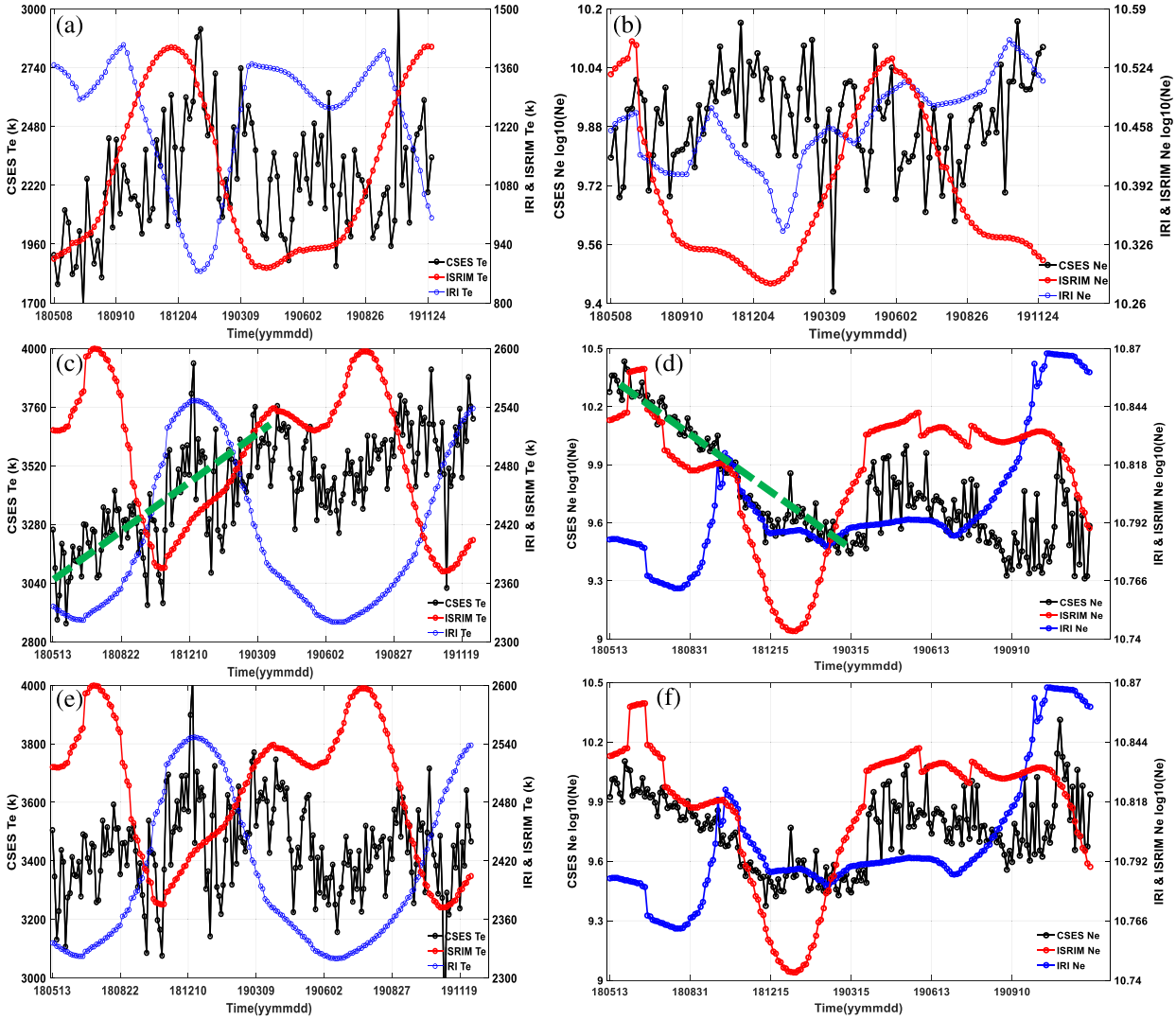

Figure 12. Comparisons of *Ne*/*Te* obtained by CSES (black), ISRIM (red), and IRI (blue); (a) nightside *Te*; (b) nightside *Ne*; (c) dayside *Te*; (d) dayside *Ne*; (e) dayside *Te* after removing the linear trend of CSES *Te*; and (f) dayside *Ne* after removing the linear trend of CSES *Ne*. Green lines are the regress trend lines.

was also observed in July 2018 (denoted by black arrows in Figures 10a and 10d). For Swarm *Te* at dayside, relatively high values are found in July 2018 than that in November 2018 at the WSA region (denoted by black arrows Figures 10d and 10e). A different feature between the two satellites is that at middle latitudes the CSES measured *Te* shows higher values in the Northern Hemisphere, while the Swarm measured *Te* shows generally the same magnitudes in two hemispheres (except in the WSA region). The relatively large *Te* measured by CSES in the Northern Hemisphere is consistent with earlier report by Liu et al. (2015) from Tatiana-2 data in which *Te* is higher in the Northern Hemisphere than that in the Southern Hemisphere during winter times.

4.2. Temporal Variations

Since it was identified only 22 simultaneous events from CSES and ISR, the long-term variation was not investigated here. Therefore, two models, ISRIM and IRI, were implemented here to further compare the temporal variation over Millstone Hill. The results of *Te* (left panels) and *Ne* (right panels) from CSES, ISRIM, and IRI are shown in Figure 12 by black, red, and blue lines, respectively. To reduce the influences caused by enhanced magnetic activity, only the periods with $Kp \leq 3$ from May 2018 to November 2019 are considered.

On the nightside the *Te* temporal variations of CSES and ISRIM are roughly consistent (Figure 12a), exhibiting an annual trend with a valley in May and peak in November, but the temporal variation of IRI *Te* is nearly opposite to the ISRIM *Te* variation. The variations of nightside *Ne* from ISRIM (Figure 12b) are generally higher in summer and lower in winter. The CSES *Ne* in November is always higher and almost at the same level in June compared to the values fromISRIM. One possible explanation is that Millstone Hill station (42.5°N, 71.5°W) is located right close to the latitudes of MIT in summer, where more MLA structures appear over it in winter (see section 4.1 for details), resulting in low values in summer while as high values in winter over Millstone Hill station.

For the dayside *Ne*/*Te* from May 2018 to April 2019, CSES *Ne* shows a general decreasing trend while the *Te* exhibits an overall increasing trend (indicated by the green dotted lines in Figures 12c and 12d). After April 2019, CSES *Ne* shows a quite sharp increase and then gradually decreases again, and the *Te* turns to the opposite way (Figures 12c and 12d). For the relative variations, we have applied a linear fit to the CSES data before April 2019 and then subtracted the linear fit from the original *Ne*/*Te* data of CSES. After the values of linear fitting have been removed, CSES *Ne* shows better agreement with ISRIM *Ne* temporal variation (Figure 12f), but the trend is quite different to the IRI predictions. After removing the linear fitting from *Te*, the variations between CSES and IRI become more consistent (Figure 12e).

It is worth to note that around November, nightside CSES *Ne* becomes larger than dayside *Ne* (see Figures 12b and 12d), due to the Millstone Hill station being possibly located in the MLA regions (Figures 8b and 9b), where *Ne* is larger on nightside than on dayside. Such variations were not seen in both IRI and ISRIM results (Figures 12b and 12d).

5. Discussions

5.1. Spatial Distribution

Our results shown in Figures 8–11 suggest that the global distribution of *Ne*/*Te* measured by CSES generally shows similar variations like the observations from Swarm B, except some regional differences. Swarm *Ne* at dayside depicts clear two-crest of EIA, while the CSES *Ne* shows a single crest somehow peaking above the equator. One reason for causing such difference is that the CSES orbit is slightly higher than Swarm B, where the two crests may not be there. At middle latitudes, the WSA can be seen from both CSES and Swarm but with a stronger relative intensity seen from CSES. However, the reason of such difference has not been well understood. One possible reason could be that the orbit of CSES is fixed in local time (around 02:00 LT on the nightside), while the orbit of Swarm B slowly drifts with local time. As revealed by Xiong and Lühr (2014), the WSA is not stationary at fixed longitude but drifts eastward with evolution of local time. Therefore, the observed WSA structure by Swarm B is slightly smoothed due to the relatively wide span of local time, which could reduce the magnitude of WSA. At subauroral region, the structures of MIT and MLA can be well recognized from the CSES and Swarm *Ne* measurements.

Another reason for explaining the difference of *Ne* measurements between CSES and Swarm is their different processing methods of LAP. CSES employed the graphical method for LAP I-V characteristic analysis; the I-V curve consists of three main regions: the ion saturation region, the electron retardation region, and the electron saturation region (Yan, Guan, et al., 2018). This method works well when the plasma distribution follows a Maxwellian distribution, without photoelectrons or secondary particles presenting and the magnetic field effects being neglected (Lebreton et al., 2006). This method is most effective to analyze the nightside I-V curves. For dayside, the ion density cannot be accurately determined, and the electron temperature may be too high due to additional ion current existing in the ion saturation and transition regions when the photoelectron current is not removed (Lebreton et al., 2006). A different method was adopted to provide the bulk of the Swarm Langmuir probe scientific data. By tracking a specific current on board, only three bias points were selected at values that were most relevant for determining plasma parameters. At these points, the bias voltage was modulated using a harmonic signal with small amplitude. The current and the complex admittance were measured at each of the three points, which is used to estimate density, temperature, and potential (Lomidze et al., 2018). The Swarm LAP selected the three bias points in advance and took these points as references to modulate the harmonic signal and obtain the final key parameters. The selected parameters could make *Ne* values stable but at the cost of the detailed information.

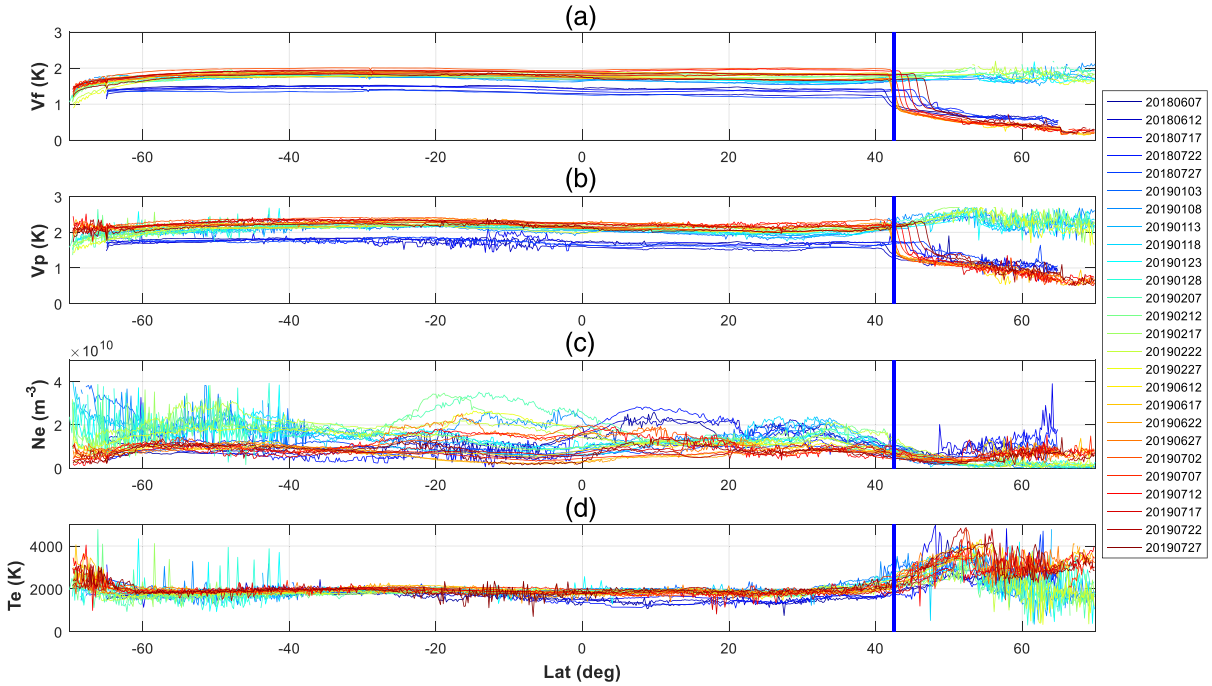

Figure 13. Latitude variation of *Vf*/*Vp*/*Ne*/*Te* denoted by revisiting orbits at nightside over the Millstone Hill station during June and July both in 2018 and 2019 and during January and February in 2019. Panel (a) is *Vf*, (b) is *Vp*, and (c) and (d) are *Ne* and *Te*, respectively.

There remain two features of *Te* that we could not interpret their causes at present. One is the anomalous increase over the WSA region at dayside in July 2018 observed both by CSES and Swarm (marked by black arrows in Figures 10a and 10d). Another peculiar observation is that of higher CSES *Te* values at dayside in the Northern Hemisphere than that in the Southern Hemisphere. Rother et al. (2010) found similar phenomenon from CHAMP electron temperature, and they suggest an interaction of the spacecraft with the ambient field as the cause for the biases of the temperature estimates. Interestingly, Swarm *Te* shows relatively similar values both at the Northern and Southern Hemispheres, while DEMETER *Te* displays a behavior that is opposite to CSES *Te*. Lomidze et al. (2018) suggested that the accuracy of satellite LAP measurements can be different from mission to mission, and the uncertainties in *Te* are usually larger than uncertainties in *Ne*. The task of finding the sources of these uncertainties is challenging for us within this study. At same time, given that *Te* has a strong dependence on the altitude and local time; it can also provide important information related to plasma movement and thermodynamic equilibrium (Ryu et al., 2016). This topic is planned to be comprehensively examined with longer data collected by CSES in the future.

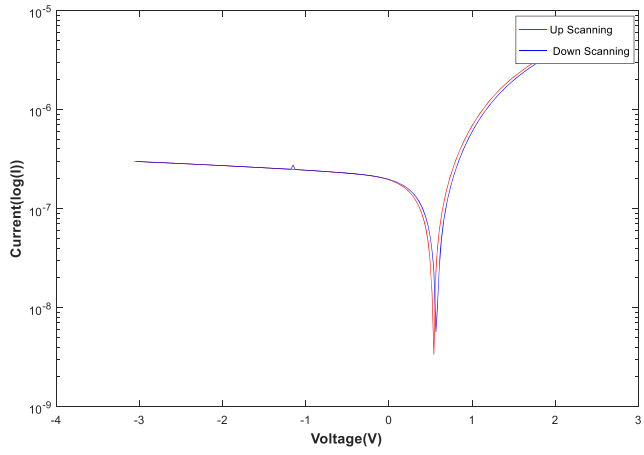

Figure 14. The I-V curves recorded by orbit 4645_0 on 4 December 2018, including up-scanning (red) and down-scanning (blue).

5.2. Temporal Variations

The temporal variation of CSES *Ne* displays a behavior that is opposite to the ISRIM predictions at nightside, which has been shown in Figure 12b. One possible reason is that the ISR at Millstone Hill is located at MIT in summer but at MLA region in winter. In addition, we also checked the data from revisiting orbits of CSES passing by the Millstone Hill station (Figure 13), and we found that the floating voltage (*Vf*) and potential voltage (*Vp*) from the LAP of CSES show sudden drops at round 42°N (Figures 13a and 13b). We confirm that this sudden drop is related to the illumination angle of the Sun, which shifts with seasons from nearly 40°N to northern polar latitudes. We conclude, therefore, that the sudden drop in *Vf*/*Vp* is caused by the strong variation in the satellite's potential when the CSES enters/leaves the shadow area. At latitudes of Millstone Hill (42.5°N), the sudden drop usually occurs from June to August. In other seasons, such as January and February, the *Vf*/*Vp* dropping

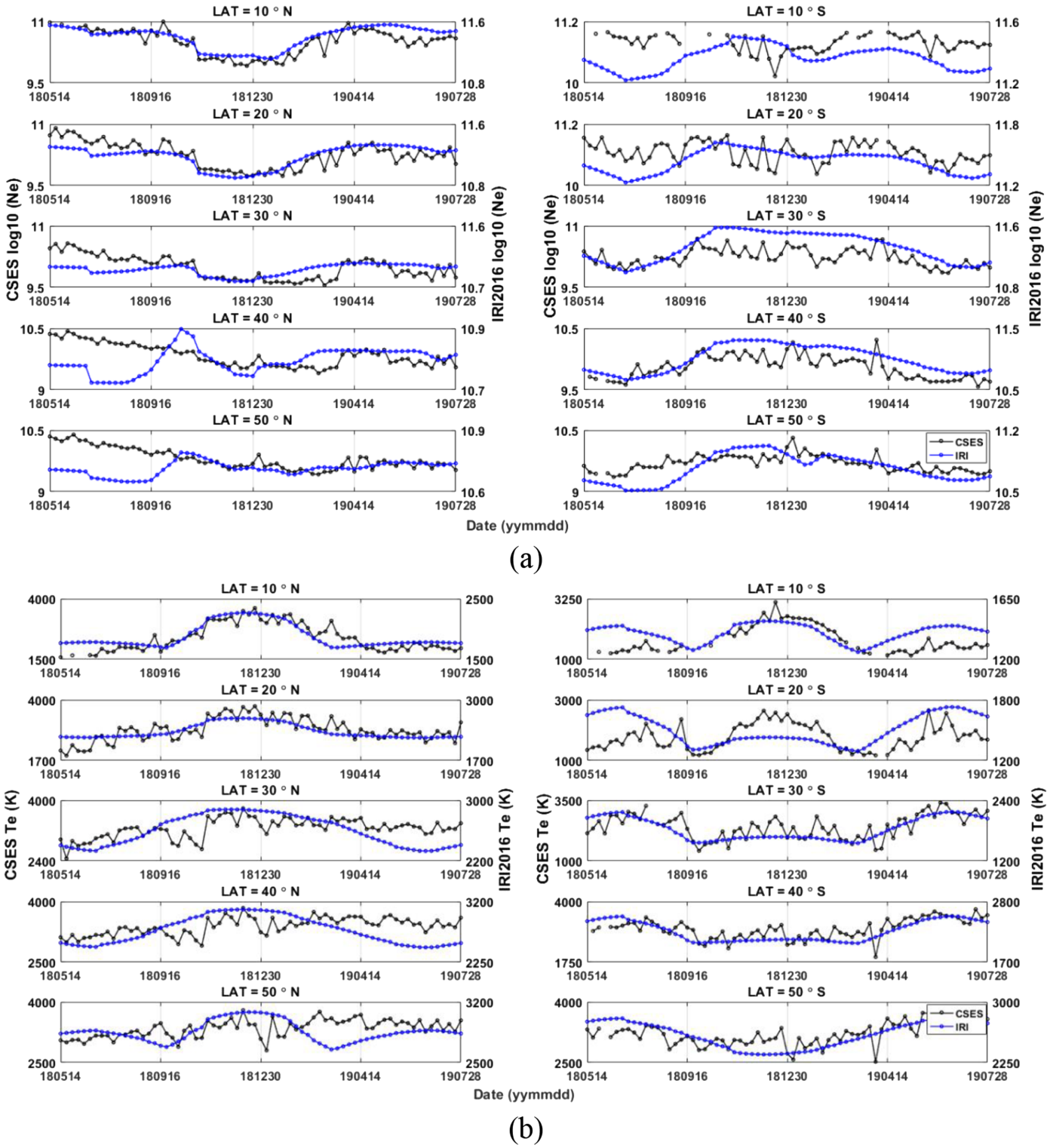

Figure 15. Temporal variations of dayside *Ne* (a) and *Te* (b) obtained by CSES and IRI 2016 at different latitudes during April 2018–July 2019 according to revisiting orbits passing by Millstone Hill. In the double coordinate system, the left vertical axis represents quantities from CSES, and the right vertical axis is the ones produced by IRI2016.

occurred at latitudes higher than 65°, which is out of the observation latitude range of LAP (the LAP of CSES is designed to switch off at latitudes higher than 65°). By comparing data with (June/July) and without (January/February) *Vf/Vp* dropping, we found that the *Ne*/*Te* showed stable variation without large difference (Figures 13c and 13d). Hence, the steep variation of satellite potential does not affect the results of data inversion, and the derived scientific data are reliable.

In addition, we found that there seems a linear trend in CSES *Ne*/*Te* at dayside (green dotted line in Figures 12c and 12d). After removing the linear trend, *Ne* obtained from CSES shows better consistent variation with the ISRIM predictions, while *Te* from CSES is more similar with the IRI predictions. We further checked the data and I-V curves and found that the down-scanning and up-scanning I-V curve fit very well (Figure 14), confirming that the probe surface treatment is chemically stable. We also compared the temporal variation at different latitudes using the revisiting orbits passing by Millstone Hill station and the corresponding IRI data at dayside. The observations at latitude 10°N/S, 20°N/S, 30°N/S, 40°N/S, and 50°N/S (Figure 15) clearly show that the temporal patterns vary with latitudes. In general, IRI *Ne*/*Te* shows a similar temporal variation trend with CSES *Ne*/*Te* except for latitudes around 30°/40°/50°N. Approximately at 30°/40°/50°N, there is a linear drift in the CSES *Ne*/*Te*, which is similar to *Ne*/*Te* variation above Millstone Hill but are not seen in the IRI *Ne*/*Te* (seen Figures 12c and 12d). Zhang et al. (2014) studied the annual variation of *Ne* in daytime and found that at latitudes from 20° to 55° the annual variation of *Ne*/*Te* in the Northern Hemisphere was not so clear with *Ne* decreasing and *Te* ascending trend during 2005–2010 in the 23rd solar cycle. The dayside *Ne*/*Te* variations at 30°/40°/50°N in this paper are very similar to those of DEMETER (Zhang et al., 2014).

Furthermore, we found that the temporal variation of the IRI *Te* is nearly opposite to the ISRIM *Te* variation both at nightside and dayside (Figures 12a and 12c). There are also large discrepancies of *Ne* at dayside during May–October 2018 between the two models (Figure 12d). In general, the model predictions show much smoother variations than the observations. Therefore, those some short-term variations may not be well reflected by the models but can be captured by the actual observations. After the linear drift in the CSES dayside *Ne*/*Te* has been removed, their temporal variations were slightly improved, when compared with the modeled results. Obviously, the daily variability not observed in the smoothed values given by the models remains.

5.3. Correlation Between CSES and Swarm

In general, the nightside/dayside *Ne* and dayside *Te* both from CSES and Swarm have a good correlation during conjunction periods, indicating that the relative variation of *Ne/Te* observed by the two satellites is consistent, despite of the fact that the absolute values of Swarm *Ne* are proportionally larger than those of CSES. It should be noted that the correlation coefficient of *Ne* during 7–16 April 2019 is not as good as other periods. By further check we found that there is rough 10° difference of longitude (at equator) for each pair orbit of CSES and Swarm B, but the longitudinal separations between them are somehow smaller during the other three conjunctions. We suggest that the larger longitudinal separation between CSES and Swarm during the conjunction in April 2019 is the reason to cause the relatively low correlation of *Ne* between them.

There is almost no correlation for *Te* between CSES and Swarm at nightside. One possible reason is that at nightside there are usually some fluctuations at the middle and low latitudes seen for the Swarm *Te*, while the CSES *Te* latitudinal profiles are much smoother. In addition, the uncertainties in *Te* are usually larger than uncertainties in *Ne* (Lomidze et al., 2018), and *Te* has a stronger dependence on the altitude and local time in general (Ryu et al., 2016). Furthermore, in section 5.2 it is found that the *Te* from IRI, ISRIM, and CSES shows quite different temporal variations in some cases. Therefore, the *Te* variation is much more complicated compared to the variation of *Ne*. Much more efforts are still needed for improving our understanding of the ionospheric *Te*, especially for the nightside.

6. Summary

In this paper, we have performed a comprehensive comparison of *Ne*/*Te* observed by CSES satellite with other measurements, for example, the ISR at Millstone Hill and Swarm B satellite. Quite good correlations and consistent global distributions are found for the *Ne*/*Te* between CSES and Swarm during their conjunction periods (except the *Te* on nightside), although that the absolute value of Swarm *Ne* is much larger than

that of CSES. The temporal variation of CSES *Ne*/*Te* is generally similar to ISRIM predictions at Millstone Hill but showing relatively large difference for the IRI predicts. The larger scale structures, like the longitudinal WN3/WN4 at equatorial and low latitudes, the WSA and MSNA at middle latitudes, and the MIT and MLA at subauroral regions, are well reflected by the CSES *Ne* data set. For *Te* measured by CSES, the well-known ETA structure at equatorial latitudes is also well depicted. This study confirms that the *Ne/Te* measurements from CSES are quite reliable and have great potentials in the scientific field of geophysics and space physics.

Data Availability Statement

CSES data can be downloaded from the website (www.leos.ac.cn). The official Swarm website and the server for Swarm data distribution are http://earth.esa.int/swarm and ftp://swarm-diss.eo.esa.int, respectively. The ISR data at Millstone Hill can be downloaded from the Madrigal database at Haystack observatory (http://madrigal.haystack.mit.edu/madrigal), the ISRIM data of ISR at Millstone Hill from the website (http://models.haystack.mit.edu/models). The IRI-2016 model code in Fortran is available from the IRI homepage at the website (irimodel.org).

Acknowledgments

This work was supported by National Key R&D Program of China (Grant no. 2018YFC1503502-06), the National Natural Science Foundation of China (Grant no. 41404058/41574139/41874174), the APSCO EARTHQUAKE Project Phase II, ISSI-BJ project: the electromagnetic data validation and scientific application research based on CSES satellite, and Special fund for public welfare of Scientific Research Project of ICD, CEA (Grant no. ZDJ2019-22). The authors would like to express special thanks to Prof. Shunrong Zhang of MIT Haystack Observatory, for his important suggestions and guidance regarding the observation and ISRIM in Millstone Hill. We greatly acknowledge Prof. Michel Parrot (LPC2E, France) for his important and helpful discussions. This work made use of the data from CSES mission, a project funded by China National Space Administration (CNSA) and China Earthquake Administration (CEA). The European Space Agency is acknowledged for providing the Swarm data. The Millstone Hill incoherent scatter radar is supported by the U.S. National Science Foundation (NSF) Geospace Facilities Program under a cooperative agreement AGS-1952737 between NSF and the Massachusetts Institute of Technology (MIT).

References

Balan, N., Oyama, K. I., Bailey, G. J., Fukao, S., Watanabe, S., & Abdu, M. A. (1997). A plasma temperature anomaly in the equatorial topside ionosphere. *Journal of Geophysical Research*, *102*(A4), 7485–7492. https://doi.org/10.1029/97JA00039

Bilitza, D., Altadill, D., Truhlik, V., Shubin, V., Galkin, I., Reinisch, B., & Huang, X. (2017). International reference ionosphere 2016: From ionospheric climate to real-time weather predictions. *Space Weather*, *15*, 418–429. https://doi.org/10.1002/2016SW001593

Chen, F. F. (2002). Langmuir Probes. In J. P. Chang (Ed.), *Principles of Plasma Processing* (pp. 79–93). New York: Plenum/Kluwer Publishers. https://doi.org/10.1007/978-1-4615-0181-7

Haagmans, R., & Mission Experts Division (2004). *The Earth's Magnetic Field and Environment Explorers-Swarm ESA SP-1279(6)* (25–26). Noordwijk, The Netherlands: ESA Publications Division c/o ESTEC.

Hargreaves, J. K. (1992). Principles of the ionosphere at middle and low latitude. In *The Solar-Terrestrial Environment. An Introduction to Geospace -the Science of the Terrestrial Upper Atmosphere, Ionosphere, and Magnetosphere* (pp. 208–210). Cambridge, UK, and New York: Cambridge University Press. https://doi.org/10.1017/CBO9780511628924

Immel, T. J., Sagawa, E., England, S. L., Henderson, S. B., Hagan, M. E., Mende, S. B., et al. (2006). Control of equatorial ionospheric morphology by atmospheric tides. *Geophysical Research Letters*, *33*, L15108. https://doi.org/10.1029/2006GL026161

Kakinami, Y., Kamogawa, M., Onishi, T., Mochizuki, K., Lebreton, J. P., Watanabe, S., et al. (2013). Validation of electron density and temperature observed by DEMETER. *Advances in Space Research*, *52*, 1267–1273. https://doi.org/10.1016/j.asr.2013.07.003

Kakinami, Y., Lin, C. H., Liu, J. Y., Kamogawa, M., Watanabe, S., & Parrot, M. (2011). Daytime longitudinal structures of electron density and temperature in the topside ionosphere observed by the Hinotori and DEMETER satellites. *Journal of Geophysical Research*, *116*, A05316. https://doi.org/10.1029/2010JA015632

Knudsen, D. J., Burchill, J. K., Buchert, S. C., Eriksson, A. I., Gill, R., Wahlund, J. E., et al. (2017). Thermal ion imagers and Langmuir probes in the swarm electric field instruments. *Journal of Geophysical Research: Space Physics*, *122*, 2655–2673. https://doi.org/10.1002/2016JA022571

Langmuir, I., & Mott-Smith, H. M. (1924). Studies of electric discharges in gases at low pressures. *General Electric Review*, *27*(7), 449–455.

Lebreton, J. P., Stverak, S., Travnicek, P., Maksimovic, M., Klinge, D., Merikallio, S., et al. (2006). The ISL Langmuir probe experiment processing onboard DEMETER: Scientific objectives, description and first results. *Planetary and Space Science*, *54*(5), 472–486. https://doi.org/10.1016/j.pss.2005.10.017

Li, Q., Hao, Y., Zhang, D., & Xiao, Z. (2018). Nighttime enhancements in the midlatitude ionosphere and their relation to the plasmasphere. *Journal of Geophysical Research: Space Physics*, *123*, 7686–7696. https://doi.org/10.1029/2018JA025422

Liu, C., Guan, Y. B., Zheng, X. Z., Zhang, A. B., Piero, D., & Sun, Y. Q. (2018). The technology of space plasma in-situ measurement on the China SeismoElectromagnetic satellite. *Science China Technological Sciences*, *62*(5), 829–838. https://doi.org/10.1007/s11431-018-9345-8

Liu, J. Y., Chang, F. Y., Oyama, K. I., Kakinami, Y., Yeh, H. C., Yeh, T. L., et al. (2015). Topside ionospheric electron temperature and density along the Weddell Sea latitude. *Journal of Geophysical Research: Space Physics*, *120*, 609–614. https://doi.org/10.1002/2014JA020227

Lomidze, L., Knudsen, D. J., Burchill, J., Kouznetsov, A., & Buchert, S. C. (2018). Calibration and validation of Swarm plasma densities and electron temperatures using ground-based radars and satellite radio occultation measurements. *Radio Science*, *53*, 15–36. https://doi.org/10.1002/2017RS006415

Lühr, H., Rother, M., Häusler, K., Fejer, B., & Alken, P. (2012). Direct comparison of non-migrating tidal signatures in the electrojet, vertical plasma drift and equatorial ionization anomaly. *Journal of Atmospheric and Solar- Terrestrial Physics*, *75–76*, 31–43. https://doi.org/10.1016/j.jastp.2011.07.009

Lühr, H., & Xiong, C. (2010). IRI-2007 model overestimates electron density during the 23/24 solar minimum. *Geophysical Research Letters*, *37*, L23101. https://doi.org/10.1029/2010GL045430

Matyjasiak, B., Przepiorka, D., & Rothkaehl, H. (2016). Seasonal variations of mid-latitude ionospheric trough structure observed with DEMETER and COSMIC. *Acta Geophysica*, *64*(6), 2734–2747. https://doi.org/10.1515/acgeo-2016-0102

McNamara, L., Cooke, D. L., Valladares, C. E., & Reinisch, B. W. (2007). Comparison of CHAMP and Digisonde plasma frequencies at Jicamarca, Peru. *Radio Science*, *42*, RS2005. https://doi.org/10.1029/2006RS003491

Oyama, K. (2015). DC Langmuir probe for measurement of space plasma: A brief review. *Journal of Astronomy and Space Sciences*, *32*(3), 167–180. https://doi.org/10.5140/JASS.2015.32.3.167

Oyama, K. I., & Hirao, K. (1976). Inaccuracies in electron density estimated due to surface contamination of Langmuir probes. *Planetary and Space Science*, *24*, 87–89. https://doi.org/10.1016/0032-0633(76)90065-9

Oyama, K. I., Lee, C. H., Fang, H. K., & Cheng, C. Z. (2012). Means to remove electrode contamination effect of Langmuir probe measurement in space. *The Review of Scientific Instruments*, *83*(5), 055113. https://doi.org/10.1063/1.4722167

Pedatella, N. M., Yue, X., & Schreiner, W. S. (2015). Comparison between GPS radio occultation electron densities and in-situ satellite observations. *Radio Science*, *50*, 518–525. https://doi.org/10.1002/2015RS005677

Rother, M., Schlegel, K., Lühr, H., & Cooke, D. (2010). Validation of CHAMP electron temperature measurements by incoherent scatter radar data. *Radio Science*, *45*, RS6020. https://doi.org/10.1029/2010RS004445

Ryu, K., Kwak, Y., Kim, Y. H., Park, J., Lee, J., & Min, K. (2016). Variation of the topside ionosphere during the last solar minimum period studied with multisatellite measurements of electron density and temperature. *Journal of Geophysical Research: Space Physics*, *121*, 7269–7286. https://doi.org/10.1002/2015JA022317

Schunk, R. W., & Nagy, A. F. (2009). Introduction. In *Ionospheres: Physics, Plasma Physics, and Chemistry* (pp. 1–10). New York: Cambridge University Press. https://doi.org/10.1017/CBO9780511635342

Shen, X. H., Zhang, X. M., Yuan, S. G., Wang, L. W., Cao, J. B., Huang, J. P., et al. (2018). The state-of-the-art of the China seismo-electromagnetic satellite mission. *Science China Technological Sciences*, *61*(5), 634–642. https://doi.org/10.1007/s11431-018-9242-02018

Xiong, C., & Lühr, H. (2013). Nonmigrating tidal signatures in the magnitude and the inter-hemispheric asymmetry of the equatorial ionization anomaly. *Annales de Geophysique*, *31*, 1115–1130. https://doi.org/10.5194/angeo-31-1115-2013

Xiong, C., & Lühr, H. (2014). The Midlatitude summer night anomaly as observed by CHAMP and GRACE: Interpreted as tidal features. *Journal of Geophysical Research: Space Physics*, *119*, 4905–4915. https://doi.org/10.1002/2014JA019959

Xiong, C., Lühr, H., & Ma, S. Y. (2013). The subauroral electron density trough: Comparison between satellite observations and IRI-2007 model estimates. *Advances in Space Research*, *51*(4), 536–544. https://doi.org/10.1016/j.asr.2011.09.021

Xiong, C., Lühr, H., Sun, L., Luo, W., Park, J., & Hong, Y. (2019). Long lasting latitudinal four peak structure in the nighttime ionosphere observed by the Swarm constellation. *Journal of Geophysical Research: Space Physics*, *124*, 9335–9347. https://doi.org/10.1029/2019JA027096

Yan, R., Guan, Y. B., Shen, X. H., Huang, J. P., Zhang, X. M., Liu, C., & Liu, D. P. (2018). The Langmuir probe onboard CSES: Data inversion analysis method and first results. *Earth and Planetary Physics*, *2*(6), 1–10. https://doi.org/10.26464/epp2018046

Yan, R., Shen, X. H., Huang, J. P., Wang, Q., Chu, W., Liu, D. P., et al. (2018). Examples of unusual ionospheric observations by the CSES prior to earthquakes. *Earth and Planetary Physics*, *2*(6), 515–526. http://doi.org/10.26464/epp2018050

Zhang, S. R., & Holt, J. M. (2004). Ionospheric plasma temperature during 1976-2001 over Millstone Hill. *Advances in Space Research*, *33*, 963–969. https://doi.org/10.1016/j.asr.2003.07.012

Zhang, S.-R., Holt, J. M., van Eyken, A. P., McCready, M., Amory-Mazaudier, C., Fukao, S., & Sulzer, M. P. (2005). Ionospheric local model and climatology from long-term databases of multiple incoherent scatter radars. *Geophysical Research Letters*, *32*, L20102. https://doi.org/10.1029/2005GL023603

Zhang, X. M. (2014). Electron density comparison between IRI2007 and DEMETER satellite data in solar minimum year. *Terrestrial, Atmospheric and Oceanic Sciences*, *25*(4), 559–571. https://doi.org/10.3319/TAO.2014.02.24.01(AA)

Zhang, X. M., Shen, X. H., Liu, J., Zeren, Z. M., Lu, Y., Ouyang, X. Y., et al. (2014). The solar cycle variation of plasma parameters in equatorial and mid latitudinal areas during 2005–2010. *Advances in Space Research*, *54*, 306–319. https://doi.org/10.1016/j.asr.2013.09.012

Zhang, Y., Paxton, L. J., & Kil, H. (2013). Nightside midlatitude ionospheric arcs: TIMED/GUVI observations. *Journal of Geophysical Research: Space Physics*, *118*, 3584–3591. https://doi.org/10.1002/jgra.50327

Zhong, J., Lei, J., Yue, X., Luan, X., & Dou, X. (2019). Middle-latitudinal band structure observed in the nighttime ionosphere. *Journal of Geophysical Research: Space Physics*, *124*, 5857–5873. https://doi.org/10.1029/2018JA026059